Mechanics of Materials 175 (2022) 104506

Contents lists available at ScienceDirect

Mechanics of Materials

journal homepage: www.elsevier.com/locate/mechmat

Tensile failure study of 3D printed PLA using DIC technique and FEM analysis

A. Sabik *, M. Rucka, A. Andrzejewska, E. Wojtczak

Department of Mechanics of Materials and Structures, Faculty of Civil and Environmental Engineering, Gdańsk University of Technology, Narutowicza 11/12, 80-233 Gdańsk, Poland

ARTICLE INFO

Keywords:
3D printed composites
PLA
Polylactic acid
Aramis
Hashin damage

ABSTRACT

The paper presents the experimental and numerical study of the failure behaviour of Fused Filament Fabricated (FFF) Polylactic Acid (PLA) samples subjected to tensile load. The examined samples are printed in flat orientation with 0°, 45° and 90° raster angles. During the experiments the deformation of the specimens is continuously scanned with the 3D Aramis measuring system utilizing the digital imaging correlation technique, enabling the determination of strain and stress distribution. In the modelling, it is assumed that each printed layer is a homogeneous transversely isotropic medium with the raster direction treated as the favoured one. The finite element models are developed in the Abaqus-Standard package. A two-dimensional equivalent single-layer approach is utilized to describe the deformation and stress state of the samples. The failure progress of the material is simulated by making use of the Hashin damage algorithm with energy-based softening, whereas the non-linear in-plane shear behaviour is included.

1. Introduction

The fourth industrial revolution, also known as Industry 4.0, is associated with the application of autonomic systems, the Internet of Things, big data, but especially results in a rising focus on additive manufacturing techniques (Galantucci et al., 2019). The techniques for processing metals (Herzog et al., 2016), ceramic materials (Deckers et al., 2014), polymeric materials (Jafferson and Chatterjee, 2021) and others can be categorized in terms of the objective of using the additive manufacturing tools. One of the most popular additive manufacturing technologies is fused filament fabrication (FFF), also referred to as fused deposition modelling (FDM), which is available and easy to use by professionals as well as by the interested consumer. The entire procedure is thermoplastic processing. The major benefit of choosing the FFF process is the manufacturing of components with no prior tooling, such as injection moulds, and it is also useful for rapid prototyping. If appropriate processing parameters are chosen, it is possible to reach strength and fatigue life similar to elements fabricated by conventional technologies (Andrzejewska et al., 2019). The additive manufacturing method can be used in the preparation of personalized models, especially in medical applications such as bone replacements, surgical templates and radiotherapy boluses (CuestaMartinez-Pañeda et al., 2019), (Seoane-Viaño et al., 2021), (Cheng et al., 2021), (Marinescu et al., 2020), (Wang et al., 2021).

In the thermoplastic polymers used in the FFF process, classification is given between biodegradable and non-biodegradable polymers. Within the group of biodegradable polymers, polylactide (PLA) is the most widely implemented. In the non-biodegradable polymer group, in contrast, acrylonitrile butadiene styrene (ABS) and polyamides (PA) are used, while the biomedical field uses PMMA or PEEK (Puppi and Chiellini, 2020). Polylactide or l-polylactic acid (PLA) is one of the most promising biomaterials in terms of the possibility to synthesize monomers from non-toxic renewable raw materials, and also because it is a naturally occurring organic acid. It is manufactured by using the glucose variety, that is dextrose received from renewable raw materials such as corn, tapioca, sugar cane and others (Masutani et al., 2014). The mechanical properties of PLA depend on stereochemistry and crystallinity. PLA is available in semi-crystalline or amorphous form, used depending on the expected strength. The semi-crystalline form is preferred when higher mechanical properties are desired (Farah et al., 2016).

Due to the increasing use of the 3D printed PLA, in recent years there has been a growing interest in its mechanical properties and numerical modelling. Since the inner arrangement of any 3D printed material corresponds to the structure of fibre-reinforced laminates, in the

* Corresponding author. Agnieszka Sabik.
E-mail address: agsa@pg.edu.pl (A. Sabik).

https://doi.org/10.1016/j.mechmat.2022.104506
Received 20 August 2022; Received in revised form 17 October 2022; Accepted 17 October 2022
Available online 22 October 2022

modelling the techniques developed for the latter ones are very often applied. Undoubtedly, a unidirectionally printed material in the macroscopic scale can be treated as a transversely isotropic medium, whereas the direction of the normal to the isotropic plane is determined by the raster angle. Thus, the constitutive relations valid for a single reinforced lamina can be employed to describe the response of the unidirectional printed material unit (Hou et al., 2020). Moreover, the mechanical properties of the fused deposition modelled materials constructed with varying raster angles in the thickness direction can be also evaluated with the methods established for the laminates. In (Magalhães et al., 2014), (Li et al., 2002), (Casavola et al., 2016), (Somireddy et al., 2020), (Somireddy and Czekanski, 2021) the in-plane stiffness properties of the 3D printed sheets were estimated with the use of the Classical Lamination Theory (CLT) and compared with the experimental values. The failure response of the 3D printed materials is frequently described with the usage of the particular laminate failure criteria (Al Abadi et al., 2018), (Verma et al., 2021), (Fernandes et al., 2021).

In this paper, the experimental and numerical investigation of the failure response of unidirectionally 3D printed PLA subjected to tensile load is presented. Different raster angles are studied. The deformation of the samples in the experiments is measured with the 3D Aramis system and digital imaging correlation (DIC) method. The experiments are simulated with the finite element software Abaqus-Standard (6.14). In the FEM approach, the printed material is handled as a multilayered composite consisting of homogeneous layers oriented along the raster direction. The deformation and stress-state of the composite are described with the use of the two-dimensional Equivalent Single Layer (ESL) concept together with the first-order shear deformation theory. The single-layer material response is assumed as elastic brittle. In the orthotropy directions, the stress-strain relations are linear whereas the in-plane shear nonlinearity is taken into account. The material degradation is modelled by making use of the Hashin damage algorithm.

2. Experimental methods

2.1. Material and sample fabrication

FFF samples used for the tensile test were printed by Ultimaker 3 Extended (Utrecht, Netherlands) with Ultimaker PLA thermoplastic material. The printer used for preparing samples has two nozzle tips with a 0.4 mm diameter. One of them is used for printing the object, while the other one can be used for support structures or printing with other material. Required printing parameters such as layer thickness, printing speed, filling rate are set in the slicing software. The Simplify 3D Printing Software was used to generate samples with three raster patterns. The geometry of FFF dog-bone specimens was designed according to ISO 527 standard. The dimensions of the samples and their visual representation such as the photograph of the typical sample are presented in Fig. 1.

In order to clearly understand the influence of fibre orientation on the selected tensile mechanical properties, samples with three different raster angles (A – 0°, B – 90°, C – 45°) in flat orientation were fabricated. The fibres were oriented with respect to the longitudinal axis of the sample and repeated on 30 layers. For each raster pattern 5 samples were manufactured, resulting in a total number of 15 samples (#A.1 – A.5, #B.1 – #B.5, #C.1 – #C.5).

To ensure the printing quality of the specimens, a layer thickness equal to 0.1 mm was used. In addition, 4 top solid layers, 4 bottom solid layers and 2 perimeter outlines were used. The temperatures adopted for the 3D printing process were around 60 °C for the building platform and 220 °C for the printing nozzle.

2.2. Measurements

Experimental investigations were performed on three groups of samples: #A.1 – A.5, #B.1 – #B.5 and #C.1 – #C.5. The experimental setup is illustrated in Fig. 2. The tensile test was conducted using Zwick/Roell Z10 universal testing machine (ZwickRoell GmbH & Co. KG, Ulm, Germany). At the beginning of the test, a preload of 10 N was applied. Then, the process of tension was performed with a constant displacement rate of 0.5 mm/min until specimen failure.

To characterize the mechanical behaviour of samples during tension, the digital image correlation (DIC) technique was applied. Images of the sample surface were captured every 2 s by ARAMIS MC 3D 12 M system (GOM GmbH, Braunschweig, Germany) equipped with two cameras of a resolution of 4096 × 3000 pixels. The collected images were processed with Aramis Professional software (GOM GmbH, Braunschweig, Germany) to analyze the deformation in the specimens during the tension test. A surface component with a facet size of 19 × 19 pixels was created for calculations of surface strains. Additionally, two virtual extensometers were set in the middle size of the specimen (Fig. 2c). Extensometer 1 had a length of 30 mm and it measured deformations in the vertical direction, while extensometer 2 with a length of 15 mm measured deformations in the horizontal direction.

3. Numerical model

It is assumed that the printed material consists of fabricated layers that are treated as a homogeneous transversely isotropic material. Such material possesses an axis of orthotropy, which is perpendicular to the isotropic plane, Fig. 3. This axis is aligned with the raster direction of the layer.

Consequently, in the modelling of material organized as described the usage of well-known laminate theories seems to be justified (Somireddy et al., 2020), (Somireddy and Czekanski, 2021), (Verma et al., 2021), (Kumar Mishra P, 2020), (Saeed et al., 2021), (Somireddy

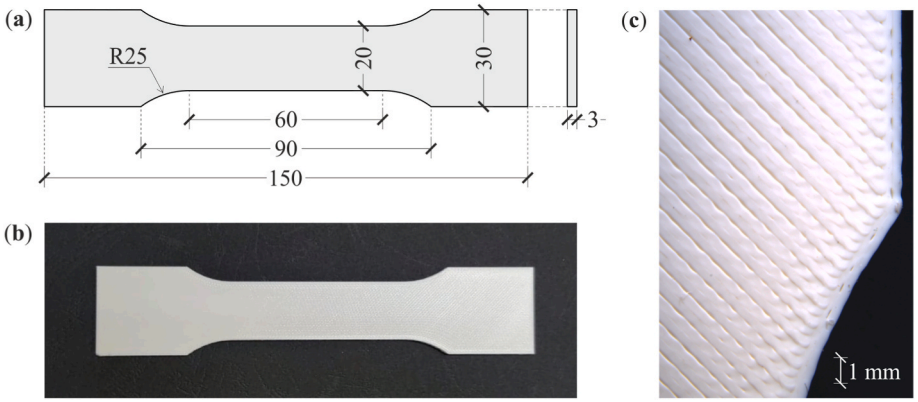

Fig. 1. Geometry of a sample (**a**), top view of the typical printed sample (**b**), and microscopic image of the sample (type #C) filling (**c**).

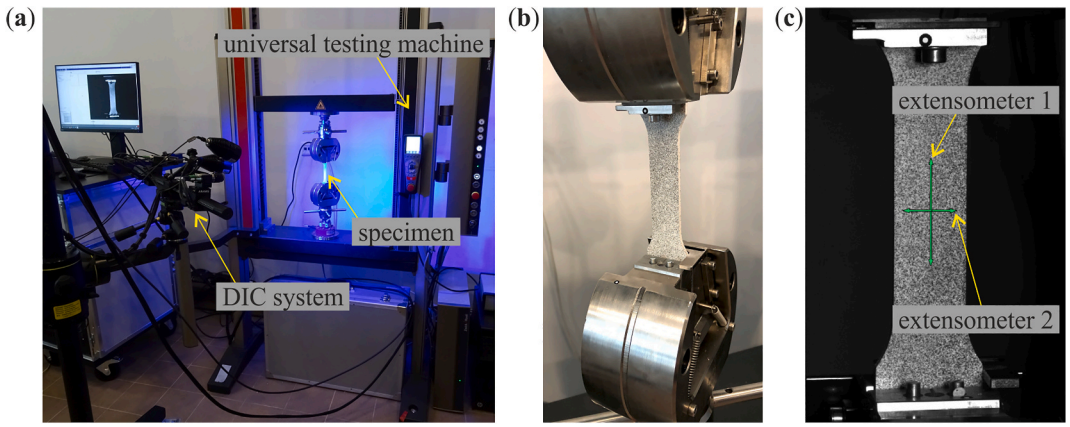

Fig. 2. Overall view of the experimental setup (a), close-up of the sample fixed into machine jaws (b), and the view from the DIC camera with virtual extensometers marked (c).

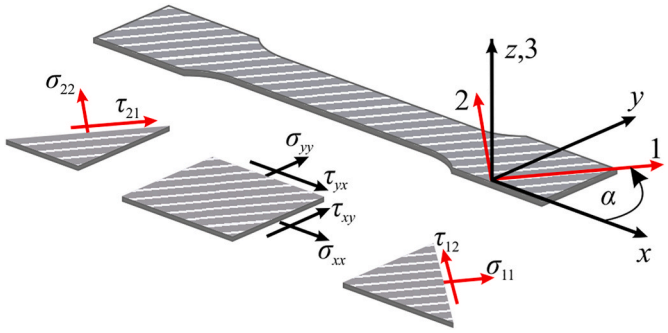

Fig. 3. Printed layer as a transversely isotropic material (α – raster angle).

et al., 2019). From the variety of the developed laminate models, the idea of so-called Equivalent Single Layer (ESL) is very useful in practice (Kreja and Sabik, 2019), (Auricchio and Sacco, 2003), with appropriate assumptions concerning the displacement distribution over the laminate thickness (Kreja and Sabik, 2019), (Abrate and Di Sciuva, 2017), (Kreja and Sabik, 2020). In fact, usually the first-order shear deformation theory (Auricchio and Sacco, 2003), (Rolfes and Rohwer, 1997) is used with linear profile of the displacement distribution over the thickness direction, and the transverse shear not neglected. Such an approach provides a good compromise between the results accuracy and computational costs in many practical problems and is implemented in many commercial codes, e.g., in Abaqus (Abaqus 6, 2080).

It is assumed that the layer material is elastic-brittle. One can contest such an assumption, since PLA, according to (Song et al., 2017), can manifest some plastic and ductile features. However, other papers reveal the brittle response (Patterson et al., 2021), (Kiendl and Gao, 2020) of this material and this was also observed in the experiments conducted in our study. Thus, the material behaviour of each layer is simulated with the Hashin-damage model. In the present work the computations are performed with, the Abaqus/Standard 6.14 software. In the following, the assumptions of the model essential for the understanding of the results and discussion are outlined.

The plane stress-strain response of the layer is governed by the constitutive matrix:

$$\mathbf{C_m} = \begin{bmatrix} c_{1111} & c_{1122} & 0 \\ c_{2211} & c_{2222} & 0 \\ 0 & 0 & c_{1212} \end{bmatrix} = \frac{1}{D} \begin{bmatrix} (1-d_1)E_1 & (1-d_1)(1-d_2)\nu_{21}E_1 & 0 \\ (1-d_1)(1-d_2)\nu_{12}E_2 & (1-d_2)E_2 & 0 \\ 0 & 0 & D(1-d_{12})G_{12}^* \end{bmatrix} \tag{1}$$

where E_1, E_2 are the longitudinal and transverse Young's moduli, respectively, ν_{12} is the Poisson ratio in the 1–2 plane, whereas $E_1\nu_{21} = E_2\nu_{12}$. G_{12}^*, G_{13}, G_{23} are the shear moduli in 1–2, 1–3 and 2–3 planes, d_1, d_2 are the damage variables in the two mutually perpendicular material directions 1, 2, respectively, $D = 1 - (1 - d_1)(1 - d_2)\nu_{12}\nu_{21}$.

The damage variables achieve values from the range $\langle 0, 1\rangle$ and can be different for compression ($d_1 \equiv d_{1c}$, d_2, d_{2c}) and tension (d_1, d_{1t}, d_2, d_{2t}) (Abaqus 6, 2080), (Lapczyk and Hurtado, 2007). The damage variable associated with the in-plane shear is evaluated from the formula

$$d_{12} = 1 - (1 - d_{1t})(1 - d_{1c})(1 - d_{2t})(1 - d_{2c}) \tag{2}$$

Since the failure behaviour of the material is to be determined, one has to notice that typically for composite materials the in-plane shear stress-strain curve is usually non-linear (Hahn and Tsai, 1973), (Van Paepegem et al., 2006), (Sabik, 2018), (Ng et al., 2010). Such observation was also made in the present experiments (specimen 45°). This nonlinearity is in contrast to the other stress components, for which, characteristically, the linear response up to the failure is identified. Therefore, it has to be emphasized, that in the present approach, in Eq. (1) the in-plane shear modulus G_{12}^* is not constant. This modulus is strain-dependent and according to (Sabik, 2018) satisfies the following relation:

$$G_{12}^* = G_{12}(1 - d_s), \textit{where} \quad d_s(\gamma_{12}) = (\gamma_{12})^{\frac{p}{\gamma_{12}+r}\ \coth(\gamma_{12}\cdot s)} \tag{3}$$

Eq. (3) provides the non-linear in-plane shear constitutive relation. The initial value of in-plane shear modulus G_{12} , i.e., valid in the range of the initial linear material response, and p, r, s parameters in Eq. (3) are obtained through the curve fitting. Such an approach together with the Hashin criterion was successfully used in (Sabik, 2019), (Chróścielewski et al., 2021) in one of the Authors' FEM codes. In Abaqus, which is adopted in this work, the non-linear in-plane shear response is implemented in the user subroutine USDFLD.

The failure initiation is identyfied according to the Hashin criterion which distinguishes two failure modes (Lapczyk and Hurtado, 2007), (Hashin, 1980):

– Failure mode in direction 1:

$$F1 = \begin{cases} F1_t = \left(\frac{\sigma_{11}}{X_t}\right)^2 + \alpha_H \left(\frac{\tau_{12}}{S_l}\right)^2 \quad for \quad \sigma_{11} \geq 0 \\ F1_c = \left(\frac{\sigma_{11}}{X_c}\right)^2 \quad for \quad \sigma_{11} < 0 \end{cases} \tag{4}$$

– Failure mode in direction 2:

$$F2 = \begin{cases} F2_t = \left(\frac{\sigma_{22}}{Y_t}\right)^2 + \left(\frac{\tau_{12}}{S_l}\right)^2 \quad for \quad \sigma_{22} \geq 0 \\ F2_c = \left(\frac{\sigma_{22}}{2S_t}\right)^2 + \left[\left(\frac{Y_c}{2S_t}\right)^2 - 1\right] \frac{\sigma_{22}}{Y_c} + \left(\frac{\tau_{12}}{S_l}\right)^2 \quad for \quad \sigma_{22} < 0 \end{cases} \tag{5}$$

where indices t and c stand for tension and compression, respectively, X_t, X_c denote the tensile and compressive strengths in direction 1, Y_t, Y_c are the tensile and compressive strengths in direction 2, S_l, S_t stand for the in-plane shear and the transverse shear strength of the layer. The α_H coefficient, taking the values 0 or 1, determines the impact of the in-plane shear stress on the tensile failure in direction 1. As the Hashin criterion does not identify the pure in-plane shear failure mode, the damage variable d_{12} (2) cannot be determined independently. Hence, it depends on the other damage variables.

If the failure onset is identified, the plane stress stiffness of the material (1) starts to be linearly reduced according to the energy-based softening algorithm (Abaqus 6, 2080), (Lapczyk and Hurtado, 2007).

4. Results and discussion

In this section, first, the experimental results are shown and discussed. Then, the comparison between the experimental and numerical results is presented.

4.1. Experimental results

The experimental stress-strain relations are presented in Fig. 4. Since the behaviour of all five specimens in each group (#A, #B, #C) is similar, to make the chart legible, the curves are marked with the same colour. First, the differences between stiffness and strength of specimens confirm that the direction of printing affects the results significantly. Samples #A (raster angle 0°) give the highest strength, reaching approximately 40 MPa, while the strength obtained for specimens #B (90°) is about four times smaller. The results for samples with a raster angle of 45° (type #C) are placed between #A and #B and give the mean strength of approximately 15 MPa. The difference in stiffness is quite similar.

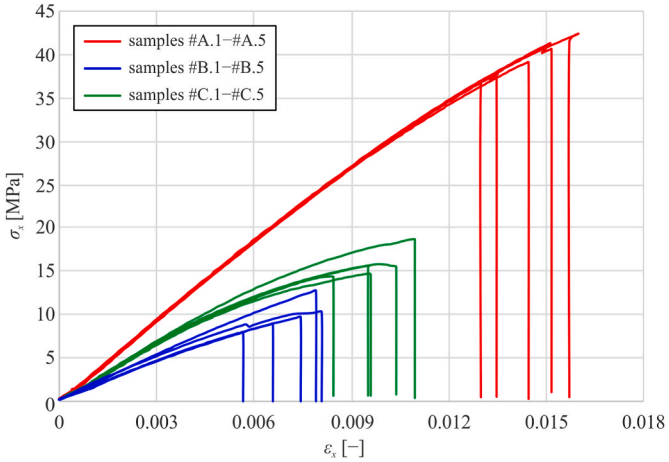

Fig. 4. Stress-strain curves for all specimens analyzed.

The tensile tests of specimens #A and #B provide the material stiffness and strength data in the orthotropy directions. The Young's modulus E_1, Poisson ratio ν_{12} and tensile strength X_t are determined from the experimental results obtained for the 0° samples (set #A.1 – #A.5). Similarly, the Young's modulus E_2 and tensile strength Y_t are taken from the experiments of 90° samples (set #B.1 – #B.5). The values of elasticity moduli are determined as a ratio of normal stress growth to the longitudinal strain growth in the range where stress-strain curves are represented by a linear relation. All these values are collected in Table 1.

The experimental results achieved for the 45° specimens (set #C.1 – #C.5) are the basis for the identification of the in-plane shear response, assuming that $\tau_{12} = \sigma_x/2 = P/(2 \cdot b \cdot t)$, $b = 20$ mm, $t = 3$ mm, and $\gamma_{12} = \varepsilon_x - \varepsilon_y$ (Somireddy et al., 2020), (Zhao et al., 2019), (JW, 1990). To capture the nonlinearity of the in-plane shear behaviour, the initial shear modulus G_{12} and constants p, r, s (see Eq. (3)), and in-plane shear strength S_l (see Eqs. (4) and (5)) are obtained through the approximation of the experimental curves $\tau_{12} - \gamma_{12}$, shown in Fig. 5.

A comment must be made as regards the in-plane shear response estimation. It is well known that the tensile test of the 45° oriented sample is an excellent method for initial shear modulus G_{12} determination (Jones, 1999), (Pindera and Herakovich, 1986). However, it is rather not recommended for the identification of the in-plane shear strength due to the relatively small contribution of the shear stresses at failure in the sample (Ganesh and Naik, 1997). The 10° off-axis test usually provides an acceptable value of this strength, since at this fibre orientation almost homogeneous shear stress state during tension is present. On the other hand, the 10° tension test is not accurate in predicting the initial shear behaviour (Pindera and Herakovich, 1986). Due to these limitations of the unidirectional 45° and 10° off-axis tests, usually in composite testing, an off-axis tensile test of symmetrically laminated bidirectional ±45° sample is performed (Van Paepegem et al., 2006), (Ng et al., 2010), (Ganesh and Naik, 1997). It provides accurate complex information about the shear response. Nonetheless, it is important to state, that in the case of the 3D printed materials the response of the bidirectional ±45° sample may be not representative for the estimation of the behaviour of the unidirectional 45° layer. It has been observed, that the measured initial stiffness of the bidirectional sample can be slightly larger than the analytical one obtained using CLT and the parameters measured for the unidirectional layer (Somireddy et al., 2019), (Somireddy et al., 2020). Taking the above into account, the Authors of this work base on 45° off-axis test but are aware, that the in-plane shear response of the material determined in this test can be not accurate beyond the initial linear range.

The photographs of all samples after tension tests are presented in Fig. 6 (left column). The observed failure patterns are clearly connected to the raster angle of each group of samples. First, while the tension force is applied along the printing direction (Fig. 6a, #A, 0°), the samples break perpendicularly to the direction of loading, near the part of the dogbones where the width changes. What is important, additional longitudinal cracks are observed. They are much more pronounced for samples #A.1, #A.3 and #A.4 and less but still visible for the two remaining ones. The distribution of Mises strain for the specimens at breakage (right column of Fig. 6a) confirms the shape of obtained failure patterns. Red fields indicating extreme strain values such as white spaces (which inform about the separation of specimen parts) are present in the locations where the horizontal and vertical cracks appear. Horizontal cracks are clearly visible for samples #A.2, #A.4 and #A.5. For sample #A.1 the moment of formation of the horizontal stress concentration

Table 1
Material data measured experimentally, $n = 5$ (Mean value ± Standard Deviation).

E_1 [MPa]	E_2 [MPa]	ν_{12} [–]	X_t [MPa]	Y_t [MPa]
2885.7 ± 17.2	1462.7 ± 131.0	0.349 ± 0.009	38.6 ± 2.07	9.59 ± 1.70

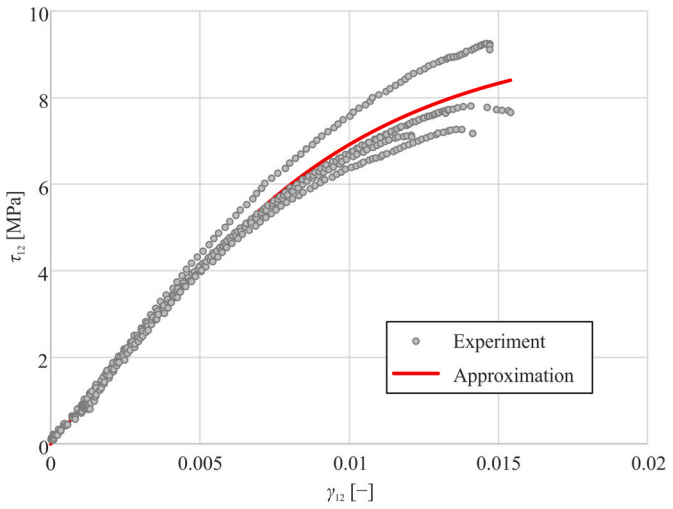

Fig. 5. Approximation of the experimental in-plane shear curves (Eq. (3)), G_{12} = 817 MPa, p = 0.12, r = 28.8, s = 1.0.

zone could have not been captured during the experiment, whereas in the case of sample #A3 the cracks appeared in the area of the sample fixed in the testing machine because of the local influence of compression applied by the testing machine jaws. Additionally, one can see some vertical lines presenting the potential locations of longitudinal cracks (between adjacent fibres) that did not turn into real cracks (not all strain concentration zones can indicate damage). It must be stressed, that the occurrence of the longitudinal cracks should be considered as a secondary effect, following the transverse crack formation (see Fig. 6a). The sudden increase of the transverse strain caused by the sample disruption induces new cracks, which, by definition, appear in the material weakening zones. In this case, these are the regions between certain raster paths, characterized by the lower tensile strength. The influence of some printing errors should also not be excluded here.

In the case of samples #B (Figs. 6b and 90°), the load is applied along the weakest material direction, thus the damage paths are perpendicular to the longitudinal sample axis and no additional cracks can be observed. The strain concentration zones are revealed in the Mises strain maps in the exact positions where breakage is observed (excluding sample #B.3, which broke beyond the area captured by Aramis). Specimens #C (Figs. 6c and 45°) break along the direction of fibres which in this case are oblique to the longitudinal sample axis. The observations of Mises strain maps agree with the real failure patterns. The location of the braking zone is clearly pointed out by the intensification of strain values. As for previous groups, one of the samples (here, #C.1) broke apart from the central part, thus the location of the breaking zone was not visualized properly.

4.2. Data for simulation

Since the ESL concept of laminate modelling is adopted, in the computations the conventional shell finite element S4 is used. Fig. 7 depicts the geometry and boundary conditions (BC) of the sample. If not specified, the conditions BC1 are imposed.

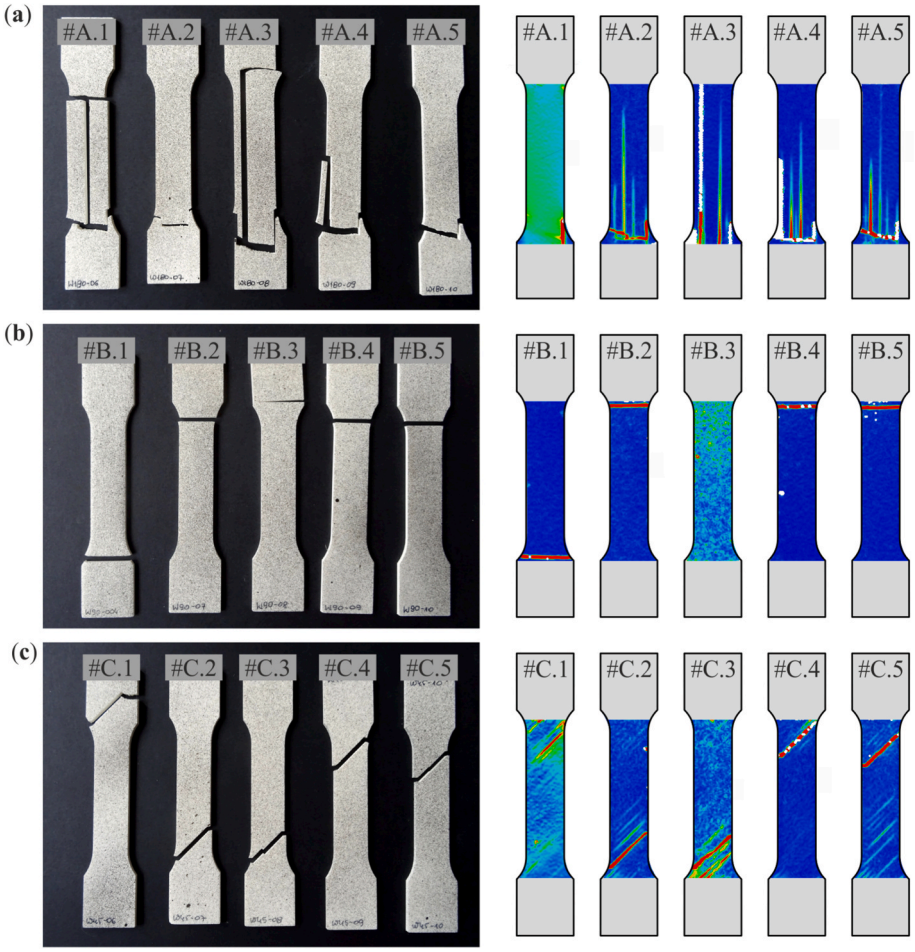

Fig. 6. Failure patterns (left column) and Mises strain maps at failure from Aramis (right column): (**a**) 0° specimens (#A.1 – #A.5); (**b**) 90° specimens (#B.1 – #B.5); (**c**) 45° specimens (#C.1 – #C.5).

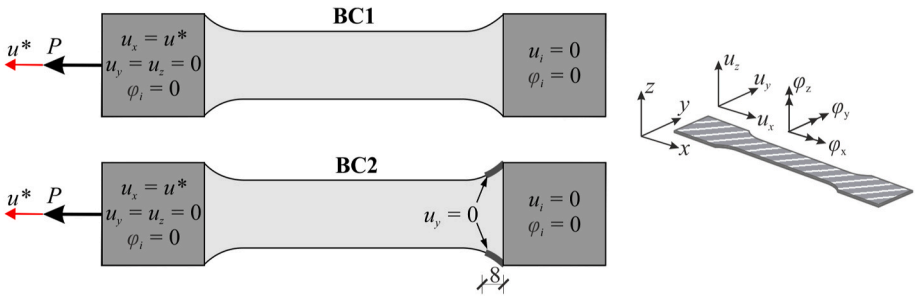

Fig. 7. Geometry of the sample and boundary conditions (BC).

Each sample consists of 30 layers. As they all are identical and only the in-plane behaviour is investigated, in the simulation one single layer with the total thickness of the entire laminate is modelled. To describe the material behaviour, assuming that it is transversely isotropic ($G_{12} = G_{13}$), 5 independent stiffness material parameters, see Eq. (1), and 5 independent strength values are required, see Eqs. (4) and (5). The Young's moduli E_1, E_2, the Poisson ratio ν_{12} and the tensile strengths X_t and Y_t are taken from the experiments (Table 1). The compressive strength values must be assumed while they cannot be obtained due to the lack of experimental data. Since in the simulations no compression is expected, these terms are assumed to be equal to the tensile strengths. The in-plane shear parameters are taken from the approximation of the experimental shear curves as described in section 4.1. The out-of-plane shear moduli are assumed to be equal, i.e. $G_{13} = G_{23} = G_{12}$. Since the experimental identification of the transverse shear strength is difficult to perform, it is assumed that $S_t = \frac{1}{2}Y_c$ (Dávila et al., 2005). If not specified, in the simulations the α_H coefficient in (4) is equal to 1.

A crucial problem concerns the estimation of the fracture energy values associated with the failure modes which control the value of the equivalent displacement at total failure, see (Lapczyk and Hurtado, 2007). The experimental determination of these energies is a problematic task (Maimi et al., 2006). Some proposals of the tests methods dedicated to their estimation are given in (Pinho, 2005). Such tests were unfortunately not conducted in the present study. In practice, the values of the fracture energies are very often assumed, e.g., on the basis of the literature data (Lapczyk and Hurtado, 2007). In this work, these terms are approximated based on the experimental data for PLA fracture energies obtained in the IZOD impact tests. In (Patterson et al., 2021), (Mishra et al., 2021), (Tezel et al., 2021), (Rajpurohit and Dave, 2021) such experiments were performed on PLA samples with various raster patterns, printing orientation, layer thickness, etc., revealing that these fabrication factors influence significantly the fracture energies. According to (Rajpurohit and Dave, 2021) the fracture energy varies between ca. 17 ÷ 32 N/mm for the 0° samples and ca. 4 ÷ 8 N/mm for 90° samples. These values were treated as the premising ones. However, by setting them for the simulation an additional restriction of the sudden drop-down of the stress-strain curves of 0° and 90° samples was imposed. Table 2 summarizes the final material data adopted in the simulation. All the viscous coefficients stabilizing the computational process are equal to $d_v = 0.0001$, see (Abaqus 6, 2080) for details.

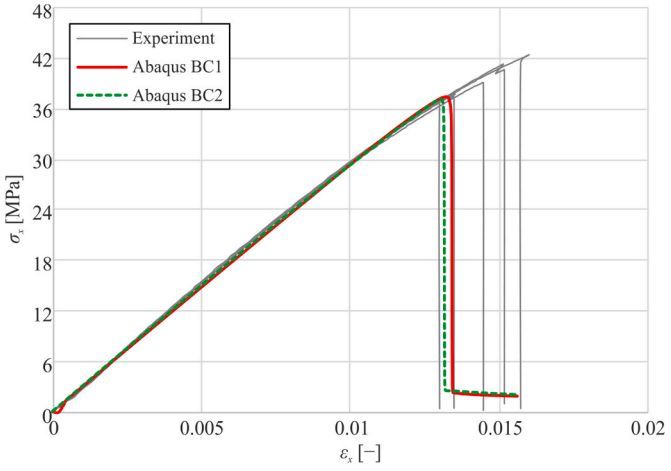

Fig. 8. Comparison of the experimental and numerical results, sample 0° (type #A).

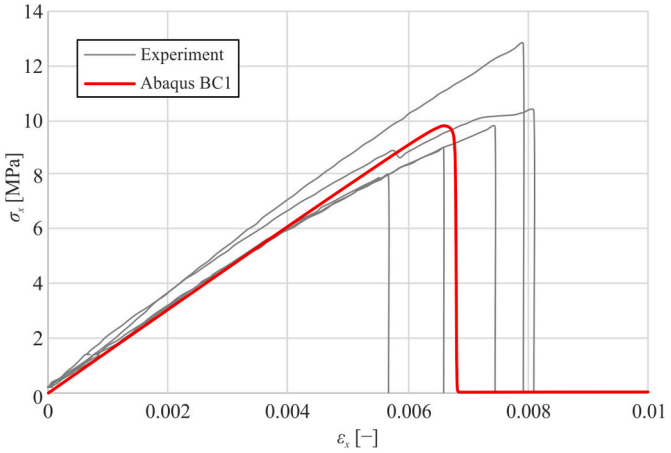

Fig. 9. Comparison of the experimental and numerical results, sample 90° (type #B).

Table 2
Material data for simulation.

Stiffness	E_1 [MPa]	E_2 [MPa]	G_{12} [MPa]	ν_{12} [–]	p [–]	r [–]	s [–]
	2890	1460	817	0.35	0.12	28.8	1.0
Strength	X_t [MPa]	X_c [MPa]	Y_t [MPa]	Y_c [MPa]	S_l [MPa]	S_t [MPa]	
	39	39	10	10	8.4	5	
Fracture energies	$G_{ft,c}$ [N/mm]	$G_{fc,c}$ [N/mm]	$G_{mt,c}$ [N/mm]	$G_{mc,c}$ [N/mm]			
	18	18	2	2			

$G_{ft,c}$, $G_{fc,c}$, $G_{mt,c}$, $G_{mc,c}$ - energies dissipated during damage for fiber tension, fiber compression, matrix tension, and matrix compression, respectively (Abaqus 6, 2080).

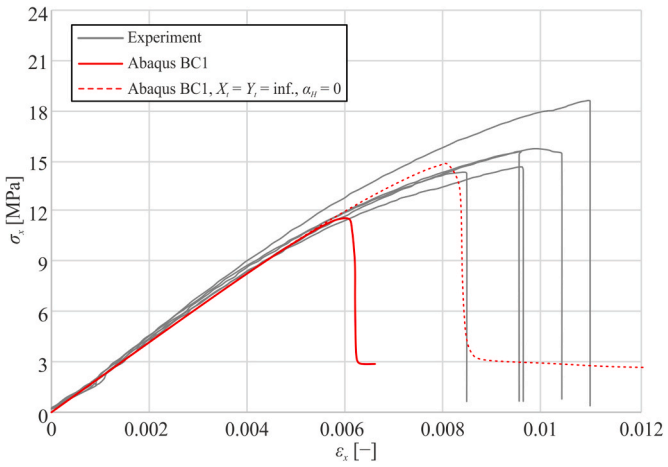

Fig. 10. Comparison of the experimental and numerical results, sample 45° (type #C).

4.3. Comparison of the numerical results with experiments

Figs. 8–10 illustrate the comparison of the numerically obtained stress-strain curves with the experimental ones. These are the relations between the engineering stress ($\sigma_x = P/(b \cdot t)$, $b = 20$ mm, $t = 3$ mm) and engineering strain measures ($\varepsilon_x = u^*/L_0$, Fig. 7).

For BC1 conditions the best agreement is observed in the case of the sample 90°. Figs. 11–13 depict the distribution of the failure indices at the load limit point and the damage variables after the failure, both corresponding to identified failure mode, in the coupons. Fig. 12a demonstrates the homogeneous stress distribution in the measuring zone of the specimen 90°. Obviously, the dominating stress component is the transverse normal stress σ_{22}. The crack of the specimen arises in this region. Such conditions provide the proper identification of the strength in direction 2 (Y_t) and consequently the agreement of the computational results with the experiment.

In contrast, Fig. 11a shows the nonhomogeneous failure index distribution. The crack of the specimen 0°, obtained experimentally and numerically, is localized in the necking zone, so in the nonhomogeneous stress region (Fig. 11a and b). This suggests, that the experimentally established tensile strength (X_t) can be underestimated. It explains partly the disagreement between the numerical and experimental results. Moreover, the crack of the sample 0° identified during the experiment is not straight as that obtained numerically, see Fig. 11b. Probably, it is due to the local stiffening of the specimen in the necking area, which is affected by the material concentration triggered by the turning back of the raster paths in this region and also due to the presence of the shape-shell surrounding the coupon. In order to approximate this stiffening, a modification of the boundary conditions was introduced into the model (BC2). It was achieved by fixing the transverse translation of the edges in the necking zone but only next to the fixed support (Fig. 7), since the primary crack was detected in this area. This fact can be possibly explained by the local material heterogeneity generated by the initiation of the printing process in this region. The

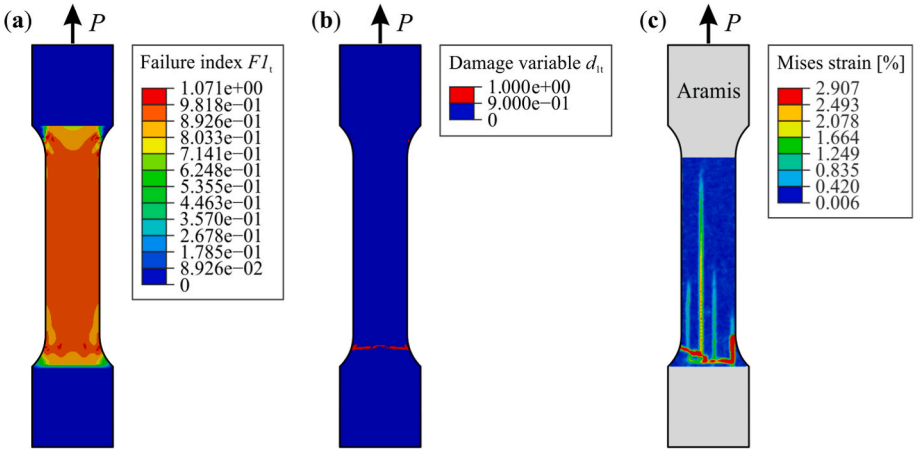

Fig. 11. Sample 0° (type #A), BC1: a) Failure index ($F1_t$) at limit point b) Damage variable (d_{1t}) after failure, c) Aramis: Mises Strain at failure (sample #A.2).

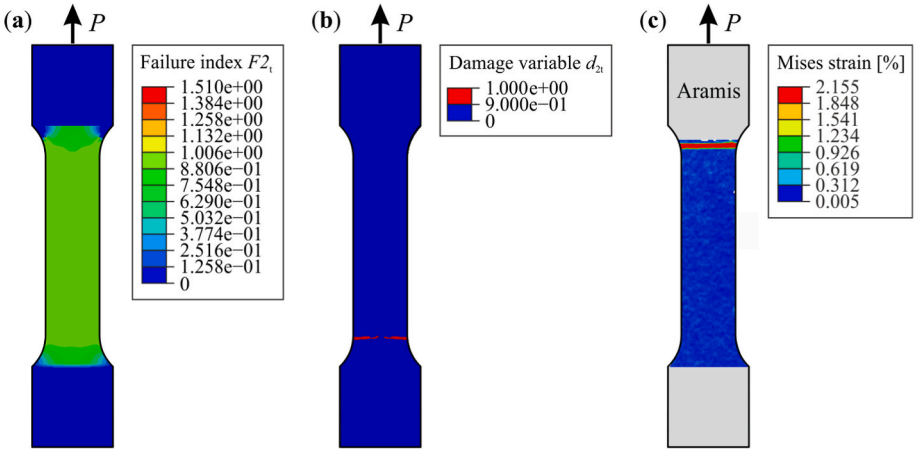

Fig. 12. Sample 90° (type #B), BC1: a) Failure index ($F2_t$) at limit point, b) Damage variable (d_{2t}) after failure, c) Aramis: Mises Strain at failure (sample #B.2).

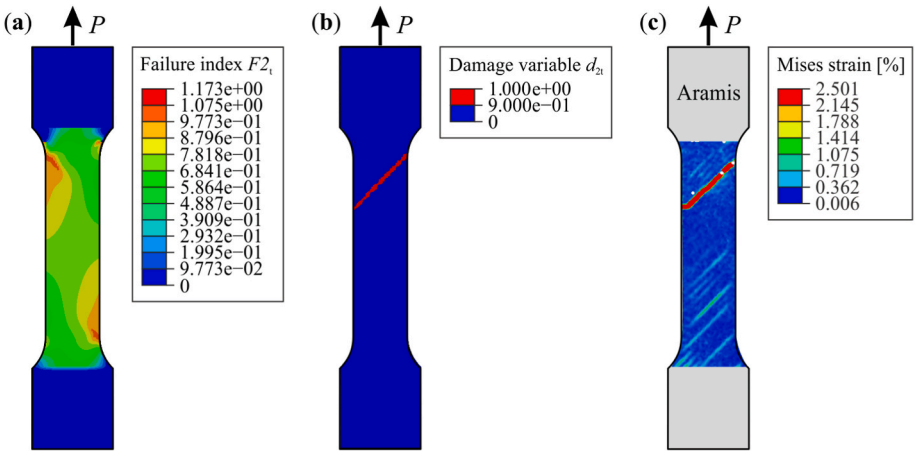

Fig. 13. Sample 45° (type #C), BC1: a) Failure index ($F2_t$) at limit point, b) Damage variable (d_{2t}) after failure, c) Aramis: Mises Strain at failure (sample #C.5).

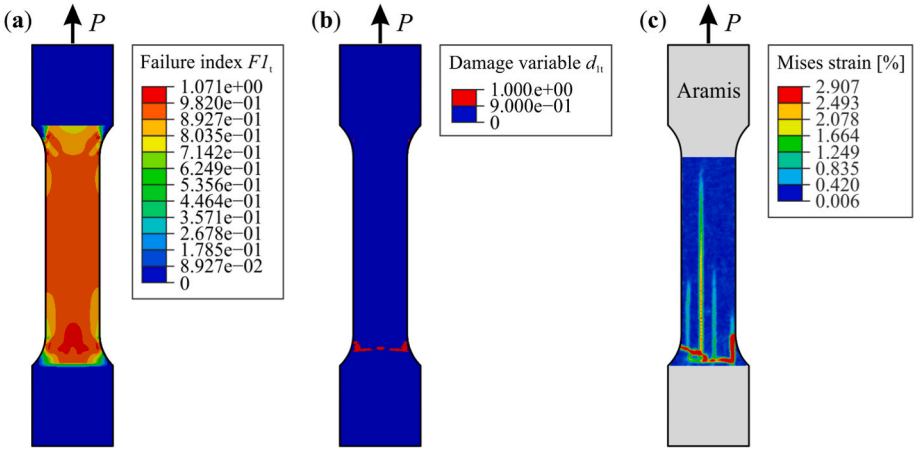

Fig. 14. Sample 0° (type #A), BC2: a) Failure index ($F1_t$) at limit point b) Damage variable (d_{1t}) after failure, c) Aramis: Mises Strain at failure (sample #A.2).

stress-strain curve does not differ significantly from that obtained for conditions BC1 (Fig. 8), but the shape of the transverse crack matches better the experimental one (Fig. 14). Nonetheless it must be stressed, that the formation of the longitudinal cracks observed experimentally is not captured by the adopted FEM model. As stated previously, these cracks follow from the significant strength differences in both orthotropy directions and possible fabrication errors. The simulation of these cracks would be a challenging task even by more sophisticated, e.g. micromechanical models.

All these observations justify the assumption that the failure response of the sample 0° is strongly dependent on its shape and fabrication technique and one should try to avoid these influences in the future.

Nonetheless, it must be stressed, that the agreement of the numerical and experimental results obtained for this sample is acceptable.

In contrary, the discrepancy observed for the specimen 45° is very high (Fig. 10). The solid series was obtained for the identified material data, i.e., that collected in Table 2. The failure pattern attained in this case is depicted in Fig. 13. The heterogeneity of the failure index distribution which corresponds to the stress field (Fig. 13a) should not be surprising in this kind of test (JW, 1990). The crack established numerically matches well the experimental observations (Fig. 13b). However, the ultimate failure stress achieved in the simulation is ca. 30% lower than the experimental value (Fig. 10). One could explain this difference by inappropriate identification of the shear curve during the experiment. As stated earlier, the 45° coupon is not the best choice for this purpose. According to (JW, 1990) the shear strength identified in such an experiment can be underestimated to a significant degree.

On the other hand, the numerical results can be very much affected by specific features of the adopted failure criterion and softening law. One must notice again, that the Hashin criterion (4), (5) does not distinguish the shear failure mode of the material. Thus, the damage variable associated with this failure mechanism (2) depends simultaneously on the damage variables corresponding to the tensile and/or compressive failure modes in both directions of orthotropy. What is more, the material softening scheme (1) is to some extent 'blind', since it does not account for the contribution of the specific stress components in the failure, e.g., if the tensile failure mode in direction 2 is identified (5), then both, the transverse normal and shear stiffness start to be reduced, even if the impact of the transverse normal stresses on failure is negligible and vice versa. A short discussion of the problem is presented in the Appendix. Taking the above into account, an additional analysis was performed with an artificially established pure shear failure condition. It was achieved by the increase of the tensile strengths in both directions (i.e., $X_t = Y_t =$ inf., in practice $X_t = Y_t = 1000$ MPa) and setting $\alpha_H = 0$.

Table 3
Comparison of ultimate tensile stress values σ_x^{ult} for samples A, B, C.

σ_x^{ult} [MPa]	Experiment	FEM	Error [%]
Sample A	39	37.4	4.1
Sample B	10	9.8	2
Sample C	16.8[a]	11.6/15	31/10.7

[a] Doubled value of the in-plane shear strength.

Thus, the failure is identified by condition (5) only, whereas, the influence of the σ_{22} stress component is negligible. This provides a remarkable increase in the ultimate stress of the coupon, see Fig. 10.

Table 3 includes the values of the ultimate tensile stress σ_x^{ult} obtained in the experiments and in simulations. The experimental values in the case of the specimens loaded in the axes of orthotropy (samples #A and #B) are equal to the tensile strength values, whereas for samples #C the ultimate tensile stress is a doubled value of the shear strength ($\tau_{12} = \sigma_x/2$). For samples #C, according to the discussion above, two FEM results are reported, (see Fig. 10). It can be observed, that the numerically evaluated ultimate stresses correspond well to the experimental ones only for the samples loaded along the axes of orthotropy (low values of error). The disagreement between the numerical and experimental results for samples #C (Fig. 10), can follow from the imprecisely identified shear strength in the experiment and specifics of the softening rule implemented in the used FEM program.

5. Conclusions

In the paper, the tensile failure response of 3D printed PLA dog-bone specimens was investigated experimentally and numerically. The coupons were fabricated in a flat position with the same printing path in each layer. Three raster angles were investigated: 0°, 45°, 90°. The Aramis system was used to scan the deformation of the coupons continuously. The numerical computations were performed in Abaqus Standard 6.14 assuming the transversely isotropic features of PLA. The brittle failure was assumed, and it was simulated by making use of the Hashin-damage model. In the orthotropy directions, the linear elastic response of the material was presumed, whereas the in-plane shear behaviour was modelled as non-linear elastic. The majority of material data was identified during the experiments. The values of the fracture energies required in the strain-softening law were taken from the literature. It was shown that the stiffness parameters of the material were identified properly since the numerical results match very well the experimental data in the initial linear response of the material. The adopted damage model captured sufficiently well the response of the samples subjected to tension along the axes of orthotropy. It was shown that slight discrepancies between the numerical and experimental data observed in the case of 0° coupon may follow from the impact of local material effects in the necking zone of the sample. This could be the reason for the underestimation of the tensile strength in the longitudinal direction of the material. In contrary to the coupons loaded in the axes of orthotropy, the failure stress and of the 45° established numerically was not consistent with the experiment. In the Authors' opinion, it is due to the underestimation of the shear strength, typical for the 45° off-axis test, and specifics of the shear stiffness softening procedure built-in Abaqus.

The authors are aware that the present study has limitations since PLA is investigated in experiments as well as in the simulations on the macro scale only. Undoubtedly, the microscale model would be more adequate for simulation of 3D printed material local effects like shape-shell surrounding the coupon, raster path turnings, etc., which were not simulated in the present work. Obviously, the micromechanical FEM model would require more detailed information about the material inner structure, like, e. g, porosity. Thus, enhanced experimental equipment would be needed. The continuum damage approach adopted in the present simulations is by definition not able to capture the internal structure of the material and therefore provides only limited information. Nonetheless, it was shown that the application of the continuum damage concept to PLA modelling seems to be justified. Perhaps, the most pronounced disagreement between the experimental and numerical results obtained for the 45° samples could be eliminated by the change of the softening rule or failure criterion in the damage model. As for now, it can be stated that the proposed approach is true for PLA samples. Taking into account that there were no tests performed with different types of samples, it is not possible to say, whether the proposed approach can be generalized for other 3D printed materials. Further works will focus on the application of a more advanced model for different geometries of specimens and various materials.

Credit author statement

Agnieszka Sabik: Conceptualization, Methodology, Software, Formal analysis, Visualisation, Writing – original draft. **Magdalena Rucka**: Conceptualization, Methodology, Formal analysis, Experimental investigations, Validation, Writing – review & editing, Supervision. **Angela Andrzejewska**: Conceptualization, Methodology, Resources, Formal analysis, Writing – original draft. **Erwin Wojtczak**: Conceptualization, Methodology, Formal analysis, Visualisation, Writing – original draft.

Declaration of competing interest

The authors declare that they have no known competing financial interests or personal relationships that could have appeared to influence the work reported in this paper.

Data availability

Data will be made available on request.

APPENDIX

In this section a discussion about the influence of the softening rule of the material shear stiffness on the FEM results is presented. Firstly, the consideration is made in relation to the AS4/3501-6 epoxy whose shear curve is properly identified without a doubt (Soden et al., 1998) and was studied by the Authors previously in (Sabik, 2019). The properties of the material are following: $E_1 = 126$ GPa, $E_2 = 11$ GPa, $G_{12} = 6.6$ GPa, $\nu_{12} = 0.28$, $X_t = 1950$ MPa, $X_c = 1480$ MPa, $Y_t = 48$ MPa, $Y_c = 200$ MPa, $S_L = 79$ MPa. The additional coefficients in the non-linear in-plane shear constitutive relation (3) are: $p = 4.14$; $r = 24.13$; $s = 46.49$ (Sabik, 2018). To simulate the shear of the material, the tension test of [45°/–45°/–45°/45°] oriented laminate with boundary conditions presented in Fig.A.1 is modelled ($\tau_{12} = P/(2 \cdot b \cdot t)$ and $\gamma_{12} = \varepsilon_x - \varepsilon_y$). The imposed lay-up and boundary conditions provide the homogeneous stress state in the coupon making the results dependent on the material properties only. The length and width of the sample are, respectively, $L = 250$ mm, $b = 25$ mm (Fig.A.1). The total thickness of the strip is $h = 2$ mm.

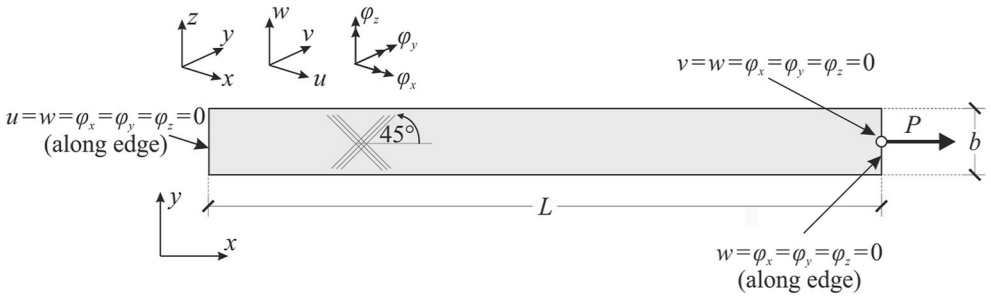

Fig. A.1. Shear test ±45°, geometry and boundary conditions.

Fig.A.2 illustrates the experimental shear curve (Soden et al., 1998) compared with present numerical result (Abaqus) and Authors' previous solution obtained with non-commercial FEM code (Sabik, 2019). In both FEM programs the same failure criterion was adopted, however, with different stiffness reduction schemes. In contrast to the softening rule implemented in Abaqus (1), in (Sabik, 2019) the in-plane shear stiffness c_{1212} (1) is reduced only if both failure modes (4) and (5) are identified. As one can observe in,Fig.A.2 this provides better agreement of the numerically evaluated ultimate shear stress with the experimental value. In contrary, in Abaqus the in-plane shear stiffness is reduced if at least one failure mode arises (2). Thus, the numerically established ultimate shear stress is underestimated. In Fig.A.3 an additional shear curve obtained with Abaqus is demonstrated, which was computed by making the assumption that $X_t = Y_t = \text{inf.}$ (in practice $X_t = Y_t = 1000$ MPa) and setting $\alpha_H = 0$. This eliminates the influence of the normal stresses in the failure conditions and imposes the deactivation of condition (4). The failure initiation is controlled by condition (5), whereas only the impact of the shear stress is taken into account. In this case the ultimate shear stress is in good agreement with the experimental data, while the failure is identified at larger shear strain and only then the shear stiffness starts to be lowered. Fig.A.4 shows a similar comparison for PLA (Fig. 5), assuming that the experimentally evaluated shear curve (Fig. 5) is the reference one. The same conclusions can be made as regards the AS4/3501-6 epoxy, however in the case of PLA the influence of the failure condition and softening rule are much more pronounced, due to the larger influence of the transverse normal stresses at failure. The contribution of particular stress components at failure is following: $(\sigma_{11}/X_t)^2 \approx 0.005$, $(\sigma_{22}/Y_t)^2 \approx 0.098$, $(\sigma_{12}/S_L)^2 \approx 0.975$ for AS4/3501-6 epoxy and $(\sigma_{11}/X_t)^2 \approx 0.05$, $(\sigma_{22}/Y_t)^2 \approx 0.27$, $(\sigma_{12}/S_L)^2 \approx 0.72$ for PLA. These observations prove that the disagreement between the numerical and experimental results obtained for dog-bone samples 45° (Fig. 10) is very much influenced by the adopted failure condition but what is more by the stiffness softening law. The range of the impact of the shear stiffness reduction on the results is dependent on the stiffness and strength data of material studied.

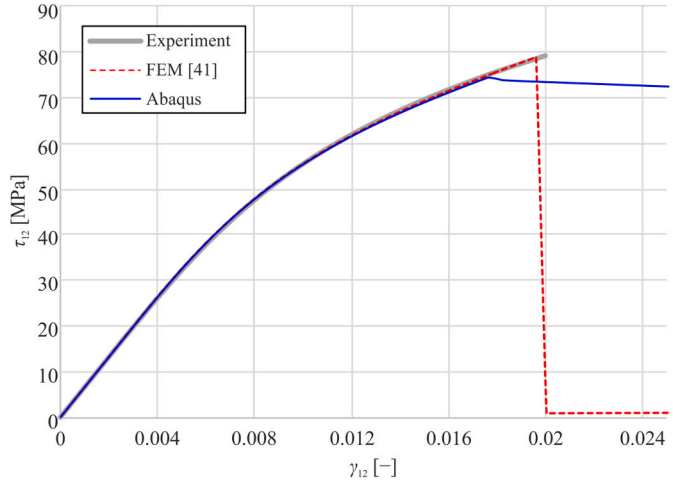

Fig. A.2. Shear test ±45° AS4/3501-6 epoxy, comparison of Abaqus and previous Authors' results.

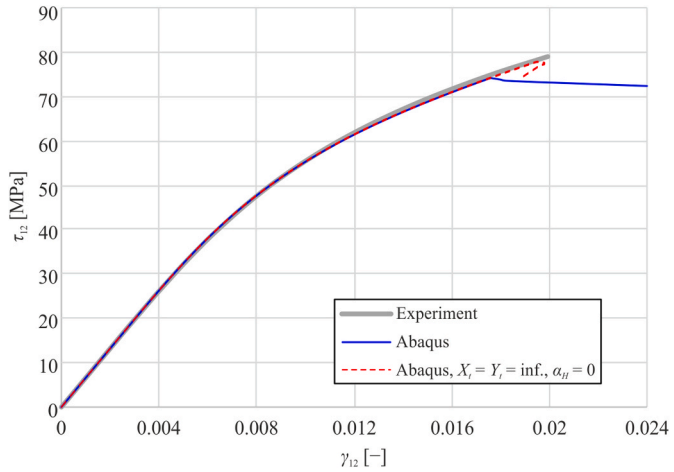

Fig. A.3. Shear test ±45° AS4/3501-6 epoxy, influence of the failure condition and softening rule in Abaqus.

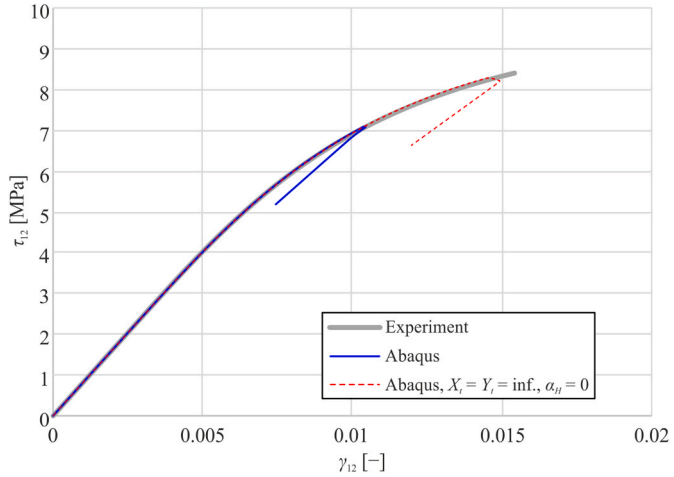

Fig. A.4. Shear test ±45° PLA, influence of the failure condition and softening rule in Abaqus.

References

Abaqus 6.14 n.d. http://130.149.89.49:2080/v6.14/.

Abrate, S., Di Sciuva, M., 2017. Equivalent single layer theories for composite and sandwich structures: a review. Compos. Struct. 179, 482–494. https://doi.org/10.1016/j.compstruct.2017.07.090.

Al Abadi, H., Thai, H.T., Paton-Cole, V., Patel, V.I., 2018. Elastic properties of 3D printed fibre-reinforced structures. Compos. Struct. 193, 8–18. https://doi.org/10.1016/j.compstruct.2018.03.051.

Andrzejewska, A., Pejkowski, L., Topoliński, T., 2019. Tensile and fatigue behavior of additive manufactured polylactide. 3D Print. Addit. Manuf. 6, 272–280. https://doi.org/10.1089/3dp.2017.0154.

Auricchio, F., Sacco, E., 2003. Refined first-order shear deformation theory models for composite laminates. J Appl Mech Trans ASME 70, 381–390. https://doi.org/10.1115/1.1572901.

Casavola, C., Cazzato, A., Moramarco, V., Pappalettere, C., 2016. Orthotropic mechanical properties of fused deposition modelling parts described by classical laminate theory. Mater. Des. 90, 453–458. https://doi.org/10.1016/j.matdes.2015.11.009.

Cheng, L., Shoma Suresh, K., He, H., Rajput, R.S., Feng, Q., Ramesh, S., et al., 2021. 3d printing of micro-and nanoscale bone substitutes: a review on technical and translational perspectives. Int. J. Nanomed. 16, 4289–4319. https://doi.org/10.2147/IJN.S311001.

Chróścielewski, J., Sabik, A., Sobczyk, B., Witkowski, W., 2021. Examination of selected failure criteria with asymmetric shear stresses in the collapse analysis of laminated shells. Compos. Struct. 261. https://doi.org/10.1016/j.compstruct.2020.113537.

Cuesta II, Martinez-Pañeda, E., Díaz, A., Alegre, J.M., 2019. The Essential Work of Fracture parameters for 3D printed polymer sheets. Mater. Des. 181, 1–9. https://doi.org/10.1016/j.matdes.2019.107968.

Dávila, C.G., Camanho, P.P., Rose, C.A., 2005. Failure criteria for FRP laminates. J. Compos. Mater. 39, 323–345. https://doi.org/10.1177/0021998305046452.

Deckers, J., Vleugels, J., Kruth, J.P., 2014. Additive manufacturing of ceramics: a review. J Ceram Sci Technol 5, 245–260. https://doi.org/10.4416/JCST2014-00032.

Farah, S., Anderson, D.G., Langer, R., 2016. Physical and mechanical properties of PLA, and their functions in widespread applications — a comprehensive review. Adv. Drug Deliv. Rev. 107, 367–392. https://doi.org/10.1016/j.addr.2016.06.012.

Fernandes, R.R., Tamijani, A.Y., Al-Haik, M., 2021. Mechanical characterization of additively manufactured fiber-reinforced composites. Aero. Sci. Technol. 113, 106653 https://doi.org/10.1016/j.ast.2021.106653.

Galantucci, L.M., Guerra, M.G., Dassisti, M., Lavecchia, F., 2019. Additive manufacturing: new trends in the 4th industrial revolution. In: Monostori, L., Majstorovic, V., Hu, S.D.D. (Eds.), Lect. Notes Mech. Eng. Springer, pp. 153–169. https://doi.org/10.1007/978-3-030-18180-2_12.

Ganesh, V.K., Naik, N.K., 1997. (±45) degree off-Axis tension test for shear characterization of plain weave fabric composites. J. Compos. Technol. Res. 19, 77–85. https://doi.org/10.1520/ctr10018j.

Hahn, H.T., Tsai, S.W., 1973. Nonlinear elastic behavior of unidirectional composite laminae. J. Compos. Mater. 7, 102–118. https://doi.org/10.1177/002199837300700108.

Hashin, Z., 1980. Failure criteria for unidirectional fiber composites. J. Appl. Mech. 47, 329–334.

Herzog, D., Seyda, V., Wycisk, E., Emmelmann, C., 2016. Additive manufacturing of metals. Acta Mater. 117, 371–392. https://doi.org/10.1016/j.actamat.2016.07.019.

Hou, Z., Tian, X., Zheng, Z., Zhang, J., Zhe, L., Li, D., et al., 2020. A constitutive model for 3D printed continuous fiber reinforced composite structures with variable fiber content. Compos. B Eng. 189, 107893 https://doi.org/10.1016/j.compositesb.2020.107893.

Jafferson, J.M., Chatterjee, D., 2021. A review on polymeric materials in additive manufacturing. Mater. Today Proc. 46, 1349–1365. https://doi.org/10.1016/j.matpr.2021.02.485.

Jones, R.M., 1999. Mechanics of Composite Materials. Taylor & Francis, USA.

JW, G. (Ed.), 1990. Composites Design Encyclopedia: Test Methods Volume VI. Technomic Publishing Company, Inc., Lancaster.

Kiendl, J., Gao, C., 2020. Controlling toughness and strength of FDM 3D-printed PLA components through the raster layup. Compos. B Eng. 180, 107562 https://doi.org/10.1016/j.compositesb.2019.107562.
Kreja, I., Sabik, A., 2019. Equivalent single-layer models in deformation analysis of laminated multilayered plates. Acta Mech. 230, 2827–2851. https://doi.org/10.1007/s00707-019-02434-7.
Kreja, I., Sabik, A., 2020. Equivalent single layer models in free vibration analysis of laminated multi-layered plates. Int. J. Struct. Stabil. Dynam. 20, 1–30. https://doi.org/10.1142/S0219455420430087.
Kumar Mishra P, P.S., 2020. Prediction of in-plane stiffness of multi-material 3D printed laminate parts fabricated by FDM process using CLT and its mechanical behaviour under tensile load. Mater. Today Commun. 23, 100955 https://doi.org/10.1016/j.mtcomm.2020.100955.
Lapczyk, I., Hurtado, J.A., 2007. Progressive damage modeling in fiber-reinforced materials. Compos Part A Appl Sci Manuf 38, 2333–2341. https://doi.org/10.1016/j.compositesa.2007.01.017.
Li, L., Sun, Q., Bellehumeur, C., Gu, P., 2002. Composite modeling and analysis for fabrication of FDM prototypes with locally controlled properties. J. Manuf. Process. 4, 129–141. https://doi.org/10.1016/S1526-6125(02)70139-4.
Magalhães, L.C., Volpato, N., Luersen, M.A., 2014. Evaluation of stiffness and strength in fused deposition sandwich specimens. J Brazilian Soc Mech Sci Eng 36, 449–459. https://doi.org/10.1007/s40430-013-0111-1.
Maimi, P., Camanho, P.P., Mayugo, J.A., Dávila, C.G., 2006. A thermodynamically consistent damage model for advanced composites. Nasa Tm 47. NASA/TM-2006-214282.
Marinescu, R., Popescu, D., Laptoiu, D., 2020. A review on 3D-printed templates for precontouring fixation plates in orthopedic surgery. J. Clin. Med. 9, 1–17. https://doi.org/10.3390/jcm9092908.
Masutani, K., Kimura, Y., 2014. PLA synthesis. From the monomer to the polymer. In: Jiménez, A., Peltzer, M., Ruseckaite, R. (Eds.), Poly(lactic Acid) Sci. Technol. Process. Prop. Addit. Appl. Royal Society of Chemistry. https://doi.org/10.1039/9781782624806-00001.
Mishra, P.K., Senthil, P., Adarsh, S., Anoop, M.S., 2021. An investigation to study the combined effect of different infill pattern and infill density on the impact strength of 3D printed polylactic acid parts. Compos. Commun. 24, 100605 https://doi.org/10.1016/j.coco.2020.100605.
Ng, W.H., Salvi, A.G., Waas, A.M., 2010. Characterization of the in-situ non-linear shear response of laminated fiber-reinforced composites. Compos. Sci. Technol. 70, 1126–1134. https://doi.org/10.1016/j.compscitech.2010.02.024.
Patterson, A.E., Pereira, T.R., Allison, J.T., Messimer, S.L., 2021. IZOD impact properties of full-density fused deposition modeling polymer materials with respect to raster angle and print orientation. Proc. Inst. Mech. Eng. Part C J Mech Eng Sci 235, 1891–1908. https://doi.org/10.1177/0954406219840385.
Pindera, M.J., Herakovich, C.T., 1986. Shear characterization of unidirectional composites with the off-axis tension test. Exp. Mech. 26, 103–112. https://doi.org/10.1007/BF02319962.
Pinho, S., 2005. Modelling composites failure laminated of using physically-based failure models. Imp Coll London 1–226.
Puppi, D., Chiellini, F., 2020. Biodegradable polymers for biomedical additive manufacturing. Appl. Mater. Today 20. https://doi.org/10.1016/j.apmt.2020.100700.
Rajpurohit, S.R., Dave, H.K., 2021. Impact strength of 3D printed PLA using open source FFF-based 3D printer. Prog Addit Manuf 6, 119–131. https://doi.org/10.1007/s40964-020-00150-6.
Rolfes, R., Rohwer, K., 1997. Improved transverse shear stresses in composite finite elements based on first order shear deformation theory. Int. J. Numer. Methods Eng. 40, 51–60. https://doi.org/10.1002/(SICI)1097-0207(19970115)40:1<51::AID-NME49>3.0.CO;2-3.
Sabik, A., 2018. Direct shear stress vs strain relation for fiber reinforced composites. Compos. B Eng. 139, 24–30. https://doi.org/10.1016/j.compositesb.2017.11.057.
Sabik, A., 2019. In-plane shear nonlinearity in failure behavior of angle-ply laminated shells. Compos. Struct. 225, 111164 https://doi.org/10.1016/j.compstruct.2019.111164.
Saeed, K., McIlhagger, A., Harkin-Jones, E., Kelly, J., Archer, E., 2021. Predication of the in-plane mechanical properties of continuous carbon fibre reinforced 3D printed polymer composites using classical laminated-plate theory. Compos. Struct. 259, 113226 https://doi.org/10.1016/j.compstruct.2020.113226.
Seoane-Viaño, I., Januskaite, P., Alvarez-Lorenzo, C., Basit, A.W., Goyanes, A., 2021. Semi-solid extrusion 3D printing in drug delivery and biomedicine: personalised solutions for healthcare challenges. J. Contr. Release 332, 367–389. https://doi.org/10.1016/j.jconrel.2021.02.027.
Soden, P.D., Hinton, M.J., Kaddour, A.S., 1998. Lamina properties, lay-up configurations and loading conditions for a range of fibre-reinforced composite laminates. Compos. Sci. Technol. 58, 1011–1022. https://doi.org/10.1016/B978-008044475-8/50003-2.
Somireddy, M., Czekanski, A., 2021. Computational modeling of constitutive behaviour of 3D printed composite structures. J. Mater. Res. Technol. 11, 1710–1718. https://doi.org/10.1016/j.jmrt.2021.02.030.
Somireddy, M., Singh, C.V., Czekanski, A., 2019. Analysis of the material behavior of 3D printed laminates via FFF. Exp. Mech. 59, 871–881. https://doi.org/10.1007/s11340-019-00511-5.
Somireddy, M., Singh, C.V., Czekanski, A., 2020. Mechanical behaviour of 3D printed composite parts with short carbon fiber reinforcements. Eng. Fail. Anal. 107, 104232 https://doi.org/10.1016/j.engfailanal.2019.104232.
Song, Y., Li, Y., Song, W., Yee, K., Lee, K.Y., Tagarielli, V.L., 2017. Measurements of the mechanical response of unidirectional 3D-printed PLA. Mater. Des. 123, 154–164. https://doi.org/10.1016/j.matdes.2017.03.051.
Tezel, T., Ozenc, M., Kovan, V., 2021. Impact properties of 3D-printed engineering polymers. Mater. Today Commun. 26, 102161 https://doi.org/10.1016/j.mtcomm.2021.102161.
Van Paepegem, W., De Baere, I., Degrieck, J., 2006. Modelling the nonlinear shear stress-strain response of glass fibre-reinforced composites. Part II: model development and finite element simulations. Compos. Sci. Technol. 66, 1465–1478. https://doi.org/10.1016/j.compscitech.2005.04.018.
Verma, P., Ubaid, J., Schiffer, A., Jain, A., Martínez-Pañeda, E., Kumar, S., 2021. Essential work of fracture assessment of acrylonitrile butadiene styrene (ABS) processed via fused filament fabrication additive manufacturing. Int. J. Adv. Manuf. Technol. 113, 771–784. https://doi.org/10.1007/s00170-020-06580-4.
Wang, X., Wang, X., Xiang, Z., Zeng, Y., Liu, F., Shao, B., et al., 2021. The clinical application of 3D-printed boluses in superficial tumor radiotherapy. Front. Oncol. 11, 1–8. https://doi.org/10.3389/fonc.2021.698773.
Zhao, Y., Chen, Y., Zhou, Y., 2019. Novel mechanical models of tensile strength and elastic property of FDM AM PLA materials: experimental and theoretical analyses. Mater. Des. 181, 108089 https://doi.org/10.1016/j.matdes.2019.108089.